PROCEEDINGS OF SPIE

Current status of Bolocam: a large-format millimeter-wave bolometer camera

Jason Glenn, Peter A. R. Ade, Mihail Amarie, James J. Bock, Samantha F. Edgington, et al.

SPIE.

Current status of Bolocam: a large-format millimeter-wave bolometer camera

Jason Glenn[a], Peter A.R. Ade[b], Mihail Amarie[c], James J. Bock[d], Samantha F. Edgington[c], Alexey Goldin[d], Sunil Golwala[c], Douglas Haig[b], Andrew E. Lange[c], Glenn Laurent[a], Philip D. Mauskopf[b], Minhee Yun[d], and Hien Nguyen[d]

[a]Center for Astrophysics & Space Astronomy, Univ. of Colorado, 389-UCB, Boulder, CO 80309
[b]Department of Physics and Astronomy, University of Wales, 5, The Parade, Cardiff, CF24 3YB
[c]Department of Physics, Caltech, MC 59-33, Pasadena, CA 91125
[d]Jet Propulsion Lab, M/S 169-327, Pasadena, CA 91109

ABSTRACT

We describe the design and performance of Bolocam, a 144-element, bolometric, millimeter-wave camera. Bolocam is currently in its commissioning stage at the Caltech Submillimeter Observatory. We compare the instrument performance measured at the telescope with a detailed sensitivity model, discuss the factors limiting the current sensitivity, and describe our plans for future improvements intended to increase the mapping speed.

Keywords: bolometers, bolometer arrays, millimeter-wave, diffraction-limited optics

1. INTRODUCTION

Bolocam is a millimeter-wave bolometer array camera for astronomical observations from the Caltech Submillimeter Observatory (CSO) and Large Millimeter Telescope. It utilizes an array of 144 Si_3N_4 micromesh bolometers with semiconductor thermistors integrated on a single wafer of silicon. We are optimizing Bolocam for large mapping speed by combining a 7.′5 field-of-view with stable, AC-biased readout electronics. The bolometer arrays are of the same type as the submillimeter bolometer arrays being fabricated for the SPIRE instrument on the Herschel Space Observatory[1]. Bolocam has 1.1 mm, 1.4 mm, and 2.1 mm bandpasses (one per observing run) selected for observations of thermal emission from cosmic dust in galaxies, from the Milky Way to high-redshift submillimeter galaxies, and observations of the Sunyaev-Zel'dovich Effect toward distant galaxy clusters.

We have had engineering runs at the CSO in all three bandpasses with a subset of bolometers and scientific observing programs have commenced. Bolocam is still evolving toward its final state, with a full complement of bolometers and fully optimized optics. In Section 2 of this paper, we describe the overall layout of Bolocam, including the closed-cycle 270 mK cryogenic system. In Section 3 we describe the bolometers. In Section 4 we describe the bias/readout electronics and data acquisition system. In Section 5, we describe the Bolocam optics. In Section 6, the performance of Bolocam to-date is described, including comparison to a comprehensive system sensitivity model.

2. CRYOGENICS AND INSTRUMENT LAYOUT

Bolocam was designed to minimize cryogenic complexity and operation at the telescope. Our design goals included a computer-controlled, closed-cycle, sub-300 mK helium sorption refrigerator, an ambient pressure (non-pumped) helium bath, 24-hour hold time, and minimal helium usage by the cryogenic amplifiers. We achieved these goals using a standard cryostat with 16-liter liquid nitrogen and helium reservoirs and a triple-stage (^{4}He/^{3}He/^{3}He) refrigerator. A schematic of the Bolocam cryostat is shown in Figure 1 accompanied by a photograph of the focal plane assembly.

The central feature of the Bolocam cryogenics is the triple-stage, closed-cycle helium refrigerator custom built for Bolocam by Chase Cryogenics. The design and operation of the refrigerator is described elsewhere[2]. The ultra-cold stage (UC) of the refrigerator, to which the bolometer array is mounted, operates at 250 mK (loaded). The intercooler
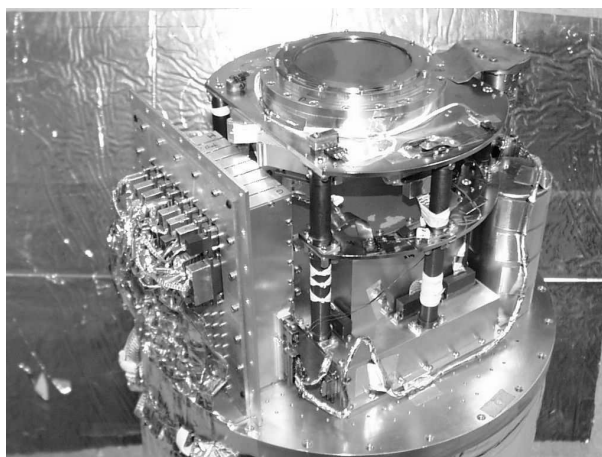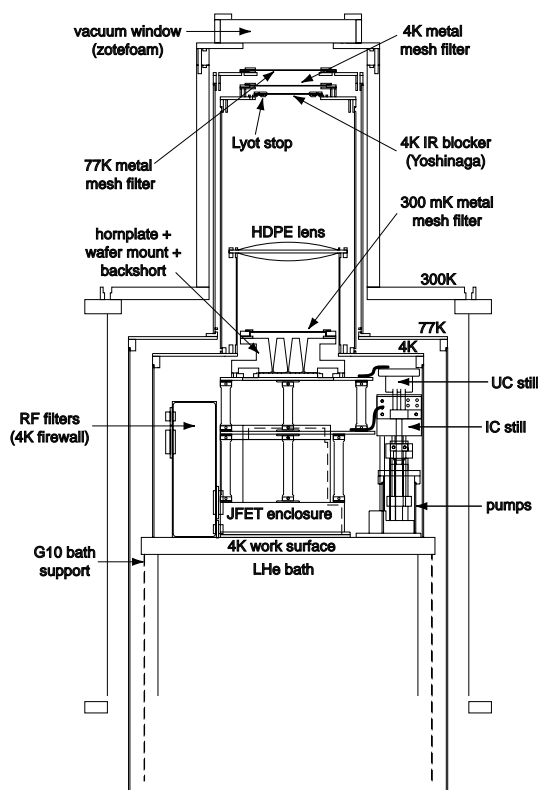
Figure 1—Left: A cross-sectional view of the Bolocam cryostat, showing the liquid He reservoir, JFET amplifier box, focal plane assembly, and cold optics. Right: A photograph of Bolocam. On top of the structure, covered by a copper-colored, metal-mesh, low-pass filter, is the bolometer array. The cables and RF filters are visible on the left and the refrigerator is visible on the right with a heat link running to the uppermost, 250 mK stage.

stage (IC) operates at 360 mK and is used to thermally intercept the UC mechanical support structure and the bolometer and thermometry wiring, sinking most of the heat load conducted from the non-pumped liquid He cold plate. The refrigerator cycle is automated and takes approximately 4 hours, including equilibration. With this configuration, the 250 mK temperature is maintained for >24 hours and the system hold time is usually limited by the capacity of the helium reservoir.

Bolocam uses cold JFETs in its electronics readout chain (see Section 4). JFETs typically exhibit their lowest voltage noise in the temperature range 100 – 150 K. To locate the JFETs near the bolometers, the JFET modules are mounted in a light-tight box within the 4.2 K space. The JFET modules are suspended from the liquid He cold plate from a fiberglass assembly and heat-sunk to the liquid N_2 reservoir through a "cold finger" that runs through the center of the liquid He reservoir. The JFETs dissipate 3.2 mW per pair, allowing them to self-heat to their optimal 140 K operating temperature.

3. BOLOMETERS

Bolocam's detector array comprises 144 micromesh "spider-web" bolometers[3] with neutron-transmutation-doped germanium (NTD) thermistors (Figure 2). The array is fabricated on a single, monolithic wafer by photolithographic methods. The thermistors are indium bump-bonded to the absorber webs prior to the final etch that removes the Si substrate beneath the webs. Each bolometer's thermal link to the thermal sink (the Si wafer substrate) is defined by metal leads deposited on one of the web support legs. The thermal conductance is controlled by the dimensions of the metal link. Bolocam currently has only 80 working detector channels. Most of the channels that do not work have non-functioning bolometers, and the remainder have failures in the load resistor or JFET packages. New fabrication and packaging techniques are expected to bring the fraction of working detectors close to 100%.

The thermal and electrical properties of the NTD-Ge based bolometers used for Bolocam can be summarized in four parameters. The first two parameters, R_0 and Δ, define the thermistor temperature-resistance relation, $R_b(T_b) = R_0 \exp \sqrt{(\Delta/T_b)}$. R_0 and Δ are determined by the doping concentration. They help determine the bolometer operating resistance and responsivity. The second two parameters, g and α, characterize the power flow through the

Proc. of SPIE Vol. 4855   31

thermal link between the bolometer and the low-temperature bath via $P = g(T_b^\alpha - T_s^\alpha)$, where P is the sum of all powers deposited in the bolometer (Joule heating and optical power) and T_b and T_s are the bolometer and bath temperatures. The thermal conductance, $G(T_b) = g\alpha T_b^{\alpha-1}$, relates a small power input dP to the resulting bolometer temperature rise dT_b via $dT_b = dP/G(T_b)$. (Note that $G(T_b)$ is frequently written as $G(T_b) = G_0(T_b/T_0)^\beta$ where T_0 is some convenient reference temperature, $G_0 = G(T_0)$, and $\beta = \alpha-1$.) G is tuned for the expected background loading and bath temperature. Since we use only one bolometer array for all three Bolocam bandpasses, we have tuned for a compromise background loading of 5-8 pW per bolometer with G(300 mK) = 100 pW/K.
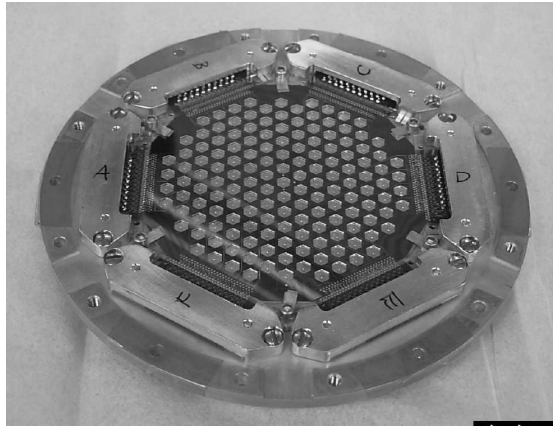

Figure 2—The Bolocam bolometer array in its mount. Fanout boards on the six sides are gold wire bonded to the detector array, with micro-D-sub connectors on the bottom. The wafer is 3 inches in diameter. It is divided into six hextants for bias and readout.

R_0, Δ, g, and α were measured from IV curves taken at multiple refrigerator base temperatures with no optical loading. In the absence of optical loading, the heat flow from the bolometer to the bath is given by $P_e = g(T_b^\alpha - T_s^\alpha)$, where T_s is the bath (sink) temperature and P_e is the Joule power dissipation. To determine g and α, the IV curves at different bath temperatures were converted to $P_e(R_b)$ curves and differenced along the P_e direction, yielding $\Delta P_e = g (T_{s2}^\alpha - T_{s1}^\alpha)$. The T_b terms cancel: R_b and thus T_b is the same for two points being differenced. These difference data were calculated for many pairs (T_{s1}, T_{s2}) and fitted to find g and α. Using the derived g and α, the $P_e(R_b)$ curves were converted to $T_b(R_b)$ curves. Curves at different base temperatures were overlaid and a linear fit to $T_b^{-1/2}$ versus ln (R) gave R_0 and Δ. Plots of Δ versus R_0 and α versus g are shown in Figure 3 with histogram of the derived G(300 mK). The bolometer parameters are summarized in Table 1. The G's fall within approximately 20% of the design value, giving a sensitivity within a few percent of optimum.
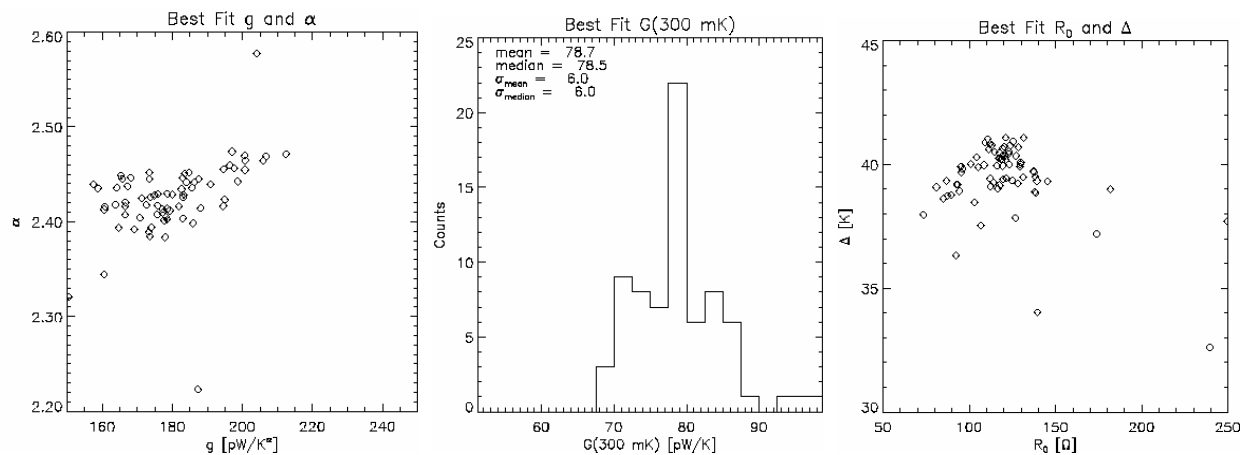

Figure 3: Bolometer parameters. Left: α versus g. Center: Thermal conductance at reference temperature of 300 mK. Right: Δ versus R_0.

Table 1—Bolometer Parameters.

We give the standard deviation of the distribution of each parameter over bolometers to indicate the pixel-to-pixel variation. The measurement uncertainties are negligible in comparison. In addition to the parameters defined in the text, we also calculate the approximate operating resistance by giving R(350 mK).

g [pW/K]	α	G(300 mK) [pW/K]	R_0 [Ω]	Δ [K]	R(350 mK) [MΩ]
190 ± 15	2.42 ± 0.04	79 ± 6	120 ± 28	39.5 ± 1.4	5.2 ± 1.3

4. READOUT ELECTRONICS

When observing faint astronomical sources at millimeter wavelengths, such as cosmic microwave background anisotropies or submillimeter galaxies, it is necessary to avoid sidelobe modulation to prevent spurious detections. Such modulation is minimized by drift-scan or slow raster-scan scan strategies. However, such scan strategies result in very slow temporal modulation of the astronomical signal. For example, it takes 4 seconds for a source to transit the FWHM (58″) of a Bolocam 2.1 mm diffraction-limited beam. Thus, excellent low-frequency stability of the readout electronics is required. We have used a fully differential, AC-stabilized, quasi-total-power readout (Figure 4).

The bolometers are biased by applying a 130 Hz sine-wave bias voltage, produced from a bandpass-filtered square wave, to the load-resistor-bolometer networks shown in Figure 4. The load resistance (10 MΩ + 10 MΩ) is significantly larger than the bolometer operating resistance (~5 MΩ), resulting in a pseudo-current bias, as is appropriate for thermistors with negative dR_b/dT_b. A common circuit supplies the bias voltage to all 144 such networks, though each hextant of 24 bolometers has its own output voltage divider and 10% amplitude trim. The bias frequency was chosen based on three criteria. It must be much faster than the bolometer time constant ($\tau \sim 10 - 20$ msec) to ensure the bolometers see an effectively constant bias power. The bias frequency must avoid electrical and thermo-mechanical microphonic resonances of the system. Finally, the bias frequency must be much slower than the RC time constant of the bolometers and wiring capacitance (R ~ few MΩ, C ~ 50-100 pF $\Rightarrow f_{-3db} \sim$ 300-600 Hz) to avoid attenuation and phase shifts arising from capacitive shunting.
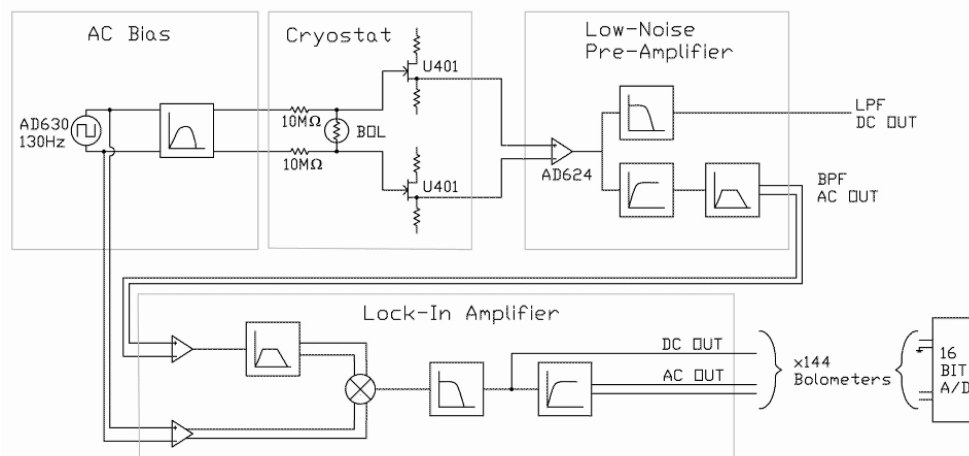

Figure 4—Simplified Bolocam electronics schematic. The bias, pre-amplifier, and lock-in amplifier electronics are all room-temperature, whereas the bolometer and load resistors are heat stationed to the 250 mK UC stage and the JFET modules self-heat to 140 K from the 77 K liquid nitrogen stage.

To further reduce susceptibiliy to electrical microphonics, RC rolloff, and RFI/EMI noise, the signals are buffered near the array using differential, unity-gain, source-follower circuits, consisting of die-mounted JFETs at 140 K. The differential output of each JFET pair travels to room temperature for further amplification. The JFET power, bolometer bias and signal, and thermometry wiring are all filtered as they enter the 4K cold space using custom-fabricated pi filters.

Once outside the dewar, the signals are amplified by low-noise instrumentation amplifiers. A low-passed version of the signal is available for bolometer and optics characterization (gain = 100, bandwidth = 10 Hz), while a version band-passed around the bias frequency is used for low-noise AC-bias operation (gain = 500, bandwidth = 3000 Hz). The AC signals are square-wave demodulated using a set of lock-in amplifier circuits, switching on the square wave used to generate the AC bias. The demodulated signal is amplified by 2.6 and low-pass filtered to provide a baseband from 0 to 20 Hz. The large DC level of this signal is proportional to the carrier amplitude, and thus to the bolometer operating resistance, and so is made available for digitization as the "DC output". The DC level is then removed using a high-pass filter (f_{-3dB} = 16 mHz) and is further amplified by 100 before digitization ("AC output"). The overall amplification is 83000 and the available signal band is 16 mHz to 20 Hz. Excellent stability has been achieved down to 10 mHz.

Each hextant possesses a bias monitor circuit, consisting of preamplifiers on the bias-generator board that view the bias voltage sent into the dewar. These signals are demodulated in the same way as bolometer signals. The low-gain lockin DC outputs thus give the rms value of the AC bias sent into the dewar, while the high-gain lockin AC outputs allow for monitoring of and corrections for fluctuations in the bias amplitude.

For each bolometer, both the low-gain DC output and the high-gain AC output signals are digitized, for a total of 288 signals. The digitizer consists of a set of 12 National Instruments SCXI-1100 multiplexer banks (32 differential inputs per bank) connected to a single fast A/D PCI card (National Instruments PCI-6034E) located inside the DAQ computer (a PC). We also record the bias monitor AC and DC lock-in amplifier outputs. Additional housekeeping signals, environmental data, and various opto-isolated telescope-related timing signals are recorded. The digitizers are read out and the data stored using a simple LabVIEW-based data-acquisition code.

5. OPTICS

The bolometers reside in integrating cavities coupled to straight-walled conical feedhorns by single-mode waveguides. While the same detector array is used for all three spectral bands, parts of the three-piece feedhorn-waveguide-cavity assembly are different for each band. The middle part of the assembly serves to mechanically support the detector array and readout wiring and is the same for all three bands. The array of feedhorns and waveguides, and the front part of the integrating cavities ("frontshorts"), are machined into the top piece, while the back part of the integrating cavities ("backshorts") are machined into the bottom piece. For the 1.1 and 1.4 mm bands, there is one feedhorn per bolometer, with opening aperture diameter 4.8 mm ($1.5 \cdot f/\# \cdot \lambda$ and $1.2 \cdot f/\# \cdot \lambda$, respectively). For the 2.1 mm configuration, fewer, larger feedhorns (37 feedhorns with 9.8 mm diameter opening apertures $\Rightarrow 1.6 \cdot f/\# \cdot \lambda$) are used to improve the per-pixel optical efficiency, while the remaining bolometers are used to monitor system drifts. Numerical simulations of the electromagnetic fields in the integrating cavities were used to optimize the cavity and absorber parameters[4].

The Bolocam feedhorn array is coupled to the CSO through a combination of on-axis optics in the cryostat (Figure 1, left panel) and ambient-temperature mirrors outside of the cryostat, converting the f/12.4 beam from the telescope to f/2.8 at the array. From the telescope, radiation is redirected by two flat mirrors onto an off-axis ellipsoidal mirror. The axes of the ellipsoid were set to optimize the image quality across the 7.′5 field-of-view using the method described by Serabyn[5]. A double-parabolic high density polyethylene lens removes most of the field curvature and focuses f/2.8 beams onto the feedhorns for a final plate scale of 7″/mm. Geometrical optics analysis yielded Strehl ratios of greater than 0.95 across the entire field-of-view, providing diffraction-limited performance in all three bands.
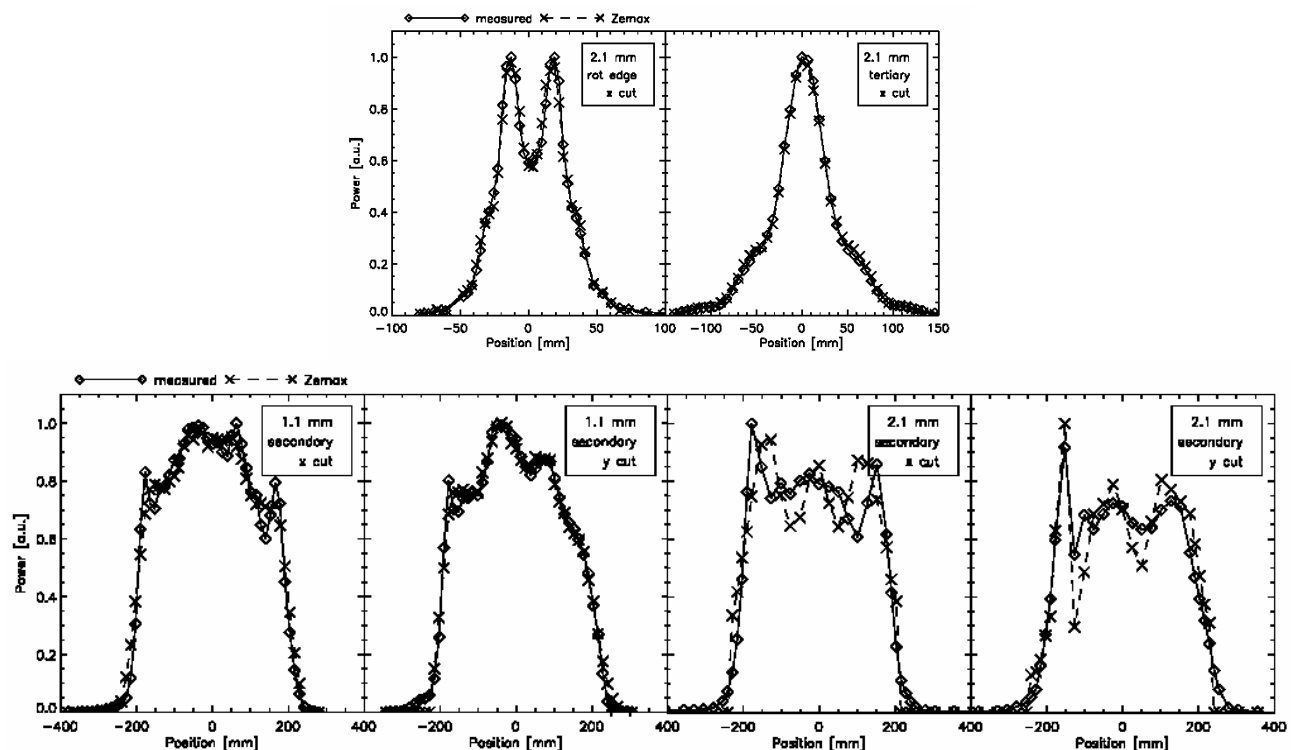
Figure 5—Comparison of measured and Zemax EE-predicted beam maps for representative pixels. Top, left: map of pixel B09 at approximately 280 mm from the dewar window. Top, right: map of pixel B09 at the ellipsoidal (tertiary) mirror. Both were taken with 2.1 mm optics. Bottom row: maps of pixel D21 at the distance of the CSO secondary (through the relay optics) using 1.1 mm and 2.1 mm optics. The data have been displaced and stretched to yield the best fit (to allow for uncertainty in the absolute position of the source used to make the maps), but the beam profiles themselves have not been modified. Note the excellent agreement on the dip and ripple features that arise from the details of the phase evolution of the beam.

The dewar window is Zotefoam (type PPA30, Zotefoams, Inc.), which has very low absorptive loss. Its index of refraction is very close to 1, rendering reflection and interference losses negligible. Out-of-band radiation is rejected by a filter stack consisting of metal mesh low-pass filters comprising layered capacitive and inductive grids, an infrared blocker, and the feedhorn waveguides.

The ellipsoidal mirror forms an image of the primary mirror on the 4.2 K window, which serves as the cold stop. In the time-reverse sense, the beams radiated by the feedhorns are truncated by the cold stop when they intercept it, with an edge taper as small as -3 dB at 1.4 mm. In the absence of diffraction, the primary illumination is expected to be given by the truncated beam. However, diffraction due to the finite size of the ellipsoidal mirror (the limiting optic in the system) results in a modified primary illumination. It is important to note here that it is diffraction at the ellipsoidal mirror, rather than at the cold stop itself, that causes the primary illumination to differ from the beams at the cold stop; were the ellipsoidal mirror and (and the flat mirrors and secondary) infinite in transverse extent, we would expect the primary illumination to match the beams at the cold stop exactly. The effect of this diffraction on the primary illumination is given approximately by convolving the cold stop intensity distribution with the diffraction kernel appropriate for the ellipsoidal mirror. The resulting primary illumination is thus a somewhat blurred version of the truncated beam at the cold stop, with ripple arising from the lobe structure of the diffraction kernel. The beams have been mapped a few inches beyond the cryostat window, at the location of the ellipsoidal mirror, at the Cassegrain focus, and at the location of the CSO secondary mirror, and compared to physical optics calculations from Zemax EE (Focus Software, Inc.), shown in Figure 5. Zemax EE does a full physical optics propagation, adjusting the grid size with the beam transverse size based on the evolution of a Gaussian pilot beam. The excellent agreement between the measured and expected beams confirms our understanding of the optics.

Because the beams in the far-field of the telescope are the Fourier transforms of the primary mirror illumination, the ripple structure on the illumination pattern has little effect in the far-field. The fairly sharp truncation of the primary mirror illumination, however, does result in ringing of the far-field beams – they are more Airy-like than gaussian. This expectation has been confirmed in all three bands with observations of planets and quasars.

6. SYSTEM PERFORMANCE AND SENSITIVITY MODEL

We have used data from laboratory testing and observations to develop and test an end-to-end instrument performance model. The model yields a detailed understanding of the instrument, and indicates what modifications promise the largest improvements in white-noise sensitivity. The observed white-noise sensitivity—noise at temporal frequencies above the sky noise—is about 20% larger than the instrument model prediction. Currently, 1/f noise, largely sky noise, limits the instrument performance at the astrophysical signal modulation frequencies (< 1 Hz).

The first component of the instrument model is the bolometer model, which was described in Section 3. The second component is the optical model, which consists of the peak-normalized spectral bandpass function $t(\nu)$, the optical efficiency, η, which provides the absolute normalization of $t(\nu)$, the effective spectral band center, ν_0, and the effective spectral bandwidth $\Delta\nu$. The non-normalized $t(\nu)$ was measured with a Fourier transform spectrometer. The spectral band center and bandwidth are given by $\Delta\nu = \int d\nu\, t(\nu)$ and $\nu_0 = [\int d\nu\, \nu\, t(\nu)] / \Delta\nu$. The optical efficiency is determined from the difference, ΔQ, in optical power detected when beam-filling hot (293K) and cold (77K) loads are placed in front of the dewar window. The optical efficiency is given by $\eta = \Delta Q / [2\, k_B\, (T_{hot} - T_{cold})\, \Delta\nu]$. ΔQ is measured by taking IV curves while viewing the hot and cold loads, converting to $P_e(R_b)$, and differencing along the P_e direction. (Note that ΔQ and the resulting optical efficiency do not depend on the bolometer model.) Averages of $t(\nu)$ over a subset of bolometers are shown in Figure 6. Histograms of η are shown in Figure 7. The median values of ν_0, $\Delta\nu$, and η and dispersion of these parameters are summarized in Table 2.

The third component of the instrument model is the optical loading, which was determined from IV curves recorded at different telescope elevations (IV curve skydips), from lab data, and from the bolometer model. The IV curves were converted to $P_e(R)$ curves, and the optical power at each elevation h, Q(h), was calculated by differencing the $P_e(R)$ curve with the Q = 0 bolometer model $P_e(R)$ curve. The Q(h) data were fit to $Q(h) = Q_0 + Q_{300}\, [1 - \exp(-\tau_z / \sin h)]$, where Q_0 is the non-atmosphere loading contribution (from the telescope and inside the cryostat), τ_z is the zenith optical depth in the band, and Q_{300} is the zenith optical loading for $\tau_z \to \infty$. It is expected that $\tau_z = a + b\, \tau_{225}$, where τ_{225} is the 225 GHz zenith optical depth measured by the CSO's 225 GHz tipper, which we monitor continuously during observations. The coefficients a and b were determined by fitting to the τ_z data from skydips taken at various τ_{225} over a given observing run. In the limit of low τ_z, we fit to the approximate relationship $Q_z = A + B\, \tau_{225}$. While τ_z is not determined for such cases, the atmospheric optical loading is. In either case, these relations allow continuous calculation of the atmospheric loading as τ_{225} varies with time (Q_0 is constant). Table 3 summarizes these optical loading parameters.

A significant fraction of the constant load (Q_0) arises from the cryostat itself. Some small loading (< 2 pW at 1.1 mm, < 1 pW at 2.1 mm) is expected due to spillover of the beam onto 4K at the cold stop. We measure the total dewar load by comparing the hot/cold load data to the IV curves expected from the bolometer model in the absence of optical loading. We find a total cryostat load of 7.3 pW [45 K] and 4.3 pW [55 K] at 1.1 mm and 2.1 mm, respectively. Possible sources of this "excess loading" are vignetting of the beam by the windows warmer than 4K, unexpected scattering of off-axis radiation into the beam by reflective surfaces inside the dewar, and unexpectedly high emissivity of the in-beam optical filters. We are currently attempting to track down and eliminate this excess load. Experience indicates that there is no reason it cannot be eliminated. Bolocam is fundamentally less sensitive to instrument emission than other instruments, such as BOOMERANG, that observe a much lower background from outside the receiver, and for which instrumental emission has been reduced to a small fraction of the emission now observed in Bolocam.
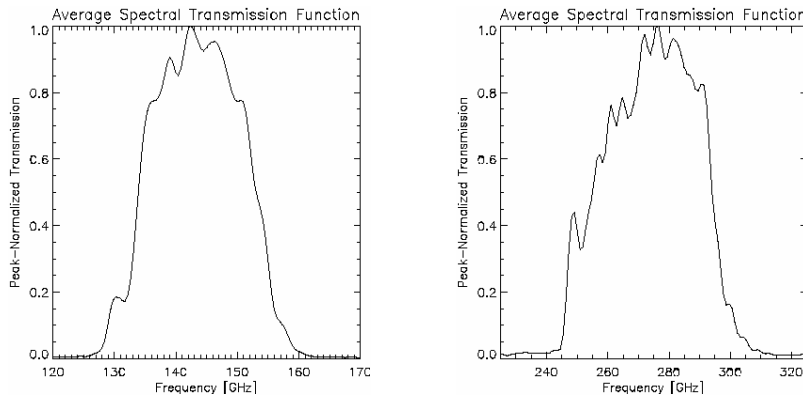
Figure 6—Peak-normalized spectral transmission averaged over a subset of bolometers. Left: 2.1 mm band. Right: 1.1 mm band.
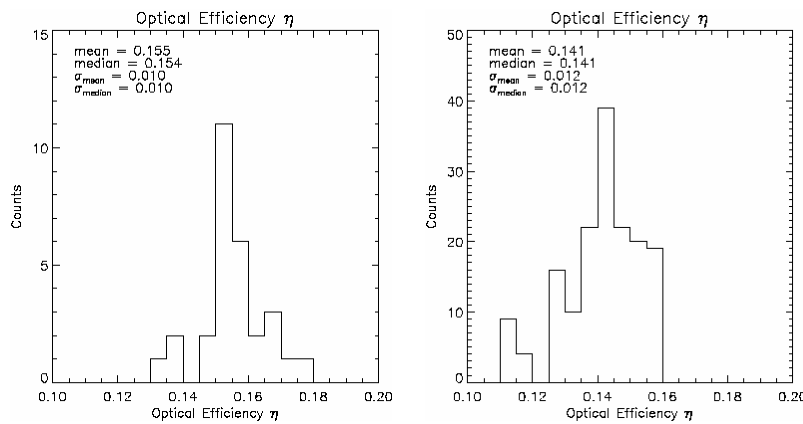

Figure 7—Optical efficiency distributions. Left: 2.1 mm band. Right: 1.1 mm band.

Table 2 – Optical Model Parameters

As for Table 1, the standard deviations given are those of the distribution of parameter values over the array.

Band	ν_0 [GHz]	$\Delta\nu$ [GHz]	η
1.1 mm	264.6 ± 1.2	42.3 ± 1.2	0.141 ± 0.012
2.1 mm	146.9 ± 1.4	18.1 ± 1.9	0.154 ± 0.010

The final components of the instrument model are the telescope efficiency, η_t, and effective telescope area, A_t. The telescope efficiency is distinct from the optical efficiency η because η is measured using loads at the cryostat window. The telescope efficiency gives the fraction of the power incident on the telescope that couples to the beam exiting the cryostat window (or, in the time reversed sense, it is the fraction of the power in the beam exiting the cryostat that makes it through the optics to the sky in the main beam).   However, η_t does not tell the whole story because the primary may be under illuminated. The telescope efficiency may be essentially unity because no beam is lost, but, from the perspective of a point source, the full geometrical area of the telescope is not used. While there are a number of methods to measure the telescope efficiency and effective area (calibrator point sources, atmospheric loading, and telescope loading among them), our data analysis is not mature enough to determine these quantities with high confidence. We have good reason to believe η_t will be well above 90%: the Zemax simulation indicates that all the optics are well

oversized, and the CSO surface roughness is known to be in the range 25-50 µm rms. We take $\eta_t = 1$ in the following, with the understanding that a better estimate of η_t is needed. A_t alone can be accurately determined from high-quality beam maps using the antenna theorem, $A_t = \lambda^2 / \Omega_{beam}$. However, accurate beam maps require proper deconvolution of the effect of the 16 mHz high-pass filter, which we have not yet accomplished. For now, we take A_t to be that given by the Zemax-predicted primary illumination, which is approximately 48 m^2, corresponding to illumination of 7.8 m of the 10.4-m diameter primary.

Table 3 – Optical Loading Parameters.

We give Q_0, Q_{300}, and coefficients a and b of the $\tau_z(\tau_{225})$ relation for the 1.1 mm band from a May, 2002, run, during which τ_{225} was high (~0.3 median), and Q_0 and the coefficients A and B of the $Q_z(\tau_{225})$ relation for the 2.1 mm band from a December, 2001, run, during which τ_{225} was low (< 0.1). Powers are also given in "cryostat-window" Rayleigh-Jeans temperature.

1.1 mm band				2.1 mm band		
Q_0	Q_{300}	a	b	Q_0	A	B
10.0 ± 1.9 [pW]	38.2 ± 4.4 [pW]	0.021 ± 0.016	1.27 ± 0.19	6.3 ± 0.8 [pW]	0.171 ± 0.045 [pW]	4.2 ± 1.4 [pW]
62 ± 16 [K]	237 ± 27 [K]			79 ± 6 [K]	2.2 ± 0.6 [K]	54 ± 18 [K]

Using the instrument model, we calculate sensitivities for comparison to observations. The most model-independent number is the observed bolometer noise-equivalent voltage (NEV) because it is directly measured. Following Mather[6] and Lamarre[7], the model NEV includes terms, added in quadrature, from bolometer Johnson noise, phonon noise, photon shot noise, photon "Bose" noise, load resistor Johnson noise, and amplifier noise. The expected value requires knowledge only of the bolometer model and optical loading model described above. The measured noise (at the bolometer) is approximately 25 nV/√Hz and is shown in Figure 8 (top spectrum); at high temporal frequencies, where sky noise and thermal drift contribute negligibly, it should approach the NEV expected from the instrument model. Figure 8 also shows two other noise spectra. The bottom spectrum is the measured room-temperature-electronics noise, approximately 8 nV/√Hz. The cold JFET noise is expected to be of the same magnitude, and the load resistor Johnson
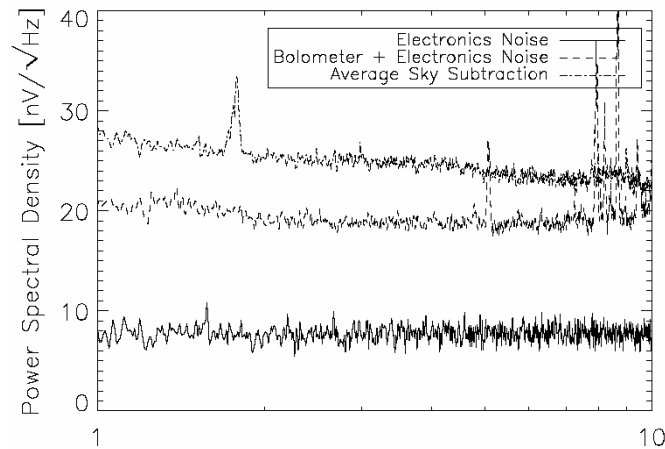

Figure 8—Power spectral densities (PSDs; averaged over the channels). Three PSDs are shown. Bottom: room-temperature electronics noise only (JFETs not included). Middle: bolometers dark but base temperature elevated to mimic operation under optical load (see text). Top: bolometer under normal operating conditions at 2.1 mm, with optical load.

noise to be negligible, giving a total of about 11 nV/√Hz total for amplifier and load resistor noises. The middle spectrum is the noise measured when the bolometers are kept dark but the base temperature is elevated and the bolometers biased so that they operate at the same current and resistance as when under optical load (done by solving $Q + gT_{s1}^{\alpha} = gT_{s2}^{\alpha}$ where T_{s1} and T_{s2} are the nominal and elevated base temperatures). Under these conditions, the Johnson, load resistor, and amplifier noises are exactly as under optical load (approximately 8, 1.5, and 11 nV/√Hz, respectively) while the phonon noise will increased by approximately √2 (to 8 nV/√Hz) due to the elevated base temperature. The measured value is about 18 nV/√Hz, consistent with the quadrature sum of the above contributions. Finally, combining all these contributions (correcting the expected phonon contribution downward by √2) and adding in the expected photon noise, we expect about 23 nV/√Hz, in good agreement with the measured 24 nV/√Hz at. While photon noise is the single most important factor, Johnson and amplifier noises are not negligible.

The observed and expected noise-equivalent powers (NEPs) are calculated by converting the measured NEV to NEP using the bolometer model. Table 4 summarizes the observed NEPs and the ratios of the measured to expected NEPs. The agreement is in general not as good as given in the above discussion, with the measured noise typically being 15–20% higher than expected.

Of more general interest are the astronomical sensitivities, given by converting the observed NEP to noise-equivalent Rayleigh-Jeans temperature (NET_{RJ}), noise-equivalent CMB temperature (NET_{CMB}), or noise-equivalent flux density (NEFD). Of particular relevance to the Bolocam science goals are two additional quantities. For distant dusty galaxies, it is useful to scale the NEFD scaled to 1mm ($NEFD_{1mm}$). We do this assuming a $\nu^{3.5}$ source spectrum. Conversely, the sensitivity to galaxy clusters via the Sunyaev-Zeldovich effect is given by the the noise-equivalent Compton y parameter (NEy). Calculation of these quantities from the observed NEP requires application of all three components of the instrument model and also correction for the atmospheric opacity. NET_{RJ} is straightforward to calculate from the NEP: $NET_{RJ} = \exp(\tau)$ NEP / [2 k_B η η_t $\Delta\nu$], where τ is the atmospheric optical depth in our spectral band and for the zenith angle at which the NEP was measured. NET_{CMB} can be calculated from NET_{RJ} using a correction factor that depends on the spectral bandpass function. NEFD can be calculated from NET_{RJ} by NEFD = (2 k_B / A_t) NET_{RJ}, where A_t is the illuminated telescope area. Finally, NEy requires a conversion from power to y parameter that depends on the spectral bandpass function, similar to the conversion from NET_{RJ} to NET_{CMB}.

It is not appropriate to simply present the sensitivities extrapolated from the measured NEP because the weather conditions for the observations we have are not typical. The historical median τ_{225} at the CSO is 0.091; at 1.1 mm, the median value for the usable data was ~0.13, while at 2.1 mm the median observed value was ~0.06. Instead, we calculate sensitivities from the instrument model for $\tau_{225} = 0.091$ and then multiply by the measured/expected NEP ratio to approximately correct the instrument model. The sensitivities calculated in this fashion are presented in Table 4.

There are two factors that currently limit the white-noise sensitivity of Bolocam. The first is the excess cryostat loading, described above. This optical loading contributes additional shot and Bose noise. Reduction of this excess load to the value expected only from spillover onto the 4K cold stop would improve the white-noise sensitivity by 25% to 30%. The second limiting factor is the unnecessarily small spectral bandwidths, especially at 2.1 mm. Both photon shot and Bose noises contribute to the NEP as sqrt(bandwidth), while any signal will increase (approximately) linearly with bandwidth, so the expected sensitivity would be improved by increasing the spectral bandwidth.

The low-frequency (<1 Hz) sensitivity that we have achieved with Bolocam in mapping speed (mapping speed $\propto$ NEFD^{-2}) is a factor of 2-3 worse than what would be expected given the per-bolometer sensitivity. The loss in sensitivity is from 1/f noise that is largely due to imperfect atmospheric subtraction and long-term instrumental drifts. The third trace in Figure 8 shows the PSD from a typical observation with sky removal implemented by simply subtracting the average of all the bolometers every sample. At high frequencies, the noise approaches the noise expected from the bolometers, electronics, and photon noise; however, at low frequencies the sky-subtracted noise exceeds the white noise. We are taking steps to reduce the 1/f noise by implementing more sophisticated sky subtraction and mapping algorithms, and possibly another form of modulation to shift the signal band to above 1 Hz, such as chopping the secondary mirror.

Table 4 – Measured and Expected Sensitivities

Definitions of quantities are given in the text. For the measured NEP and the measured/expected ratios, the standard deviation given is that of the distribution over bolometers. For the remainder of the quantites, we choose the median instrument model parameters and apply the median measured/expected correction as described in the text. The large NET_{CMB} and NEy at 1.1 mm and the large $NEFD_{1mm}$ at 2.1 mm reflect the facts that the 1.1 mm band is not ideal for CMB and SZ work, and likewise the 2.1 mm is unsuitable for galaxy searches.

Quantity	1.1 mm band	2.1 mm band
Measured NEP [aW/√Hz]	103 ± 50	103 ± 20
Measured/Expected NEP	1.22 ± 0.14	1.14 ± 0.14
NET_{RJ} [mK_{RJ} √sec]	0.98	0.92
NET_{CMB} [mK_{CMB} √sec]	4.56	1.55
NEy [10^{-3} √sec]	1.12	0.57
NEFD [mJy √sec]	56	54
$NEFD_{1mm}$ [mJy √sec]	86	670

7. CONCLUSION

Bolocam has entered is commissioning phase at the CSO. The measured performance is consistent with a detailed instrument model that takes into account 1/f noise, excess optical loading arising inside the cryostat, and less than 100% yield in electronics and bolometers. We are currently implementing solutions to each of these problems, and expect the mapping speed to improve substantially in the near future.

8. ACKNOWLEDGEMENTS

9. REFERENCES

1. M.J. Griffin, B.M. Swinyard, and L. Vigroux, "The SPIRE Instrument for Herschel", Proc. Symp. The Promise of the Herschel Space Observatory, pp. 37-44, 2000.
2. R.S. Bhatia, S.T. Chase, S.F. Edgington, J. Glenn, W.C. Jones, A.E. Lange, B. Maffei, A.K. Mainzer, P.D. Mauskopf, B.J. Philhour, and B.K. Rownd, "A Three-Stage Helium Sorption Refrigerator for Cooling of Infrared Detectors to 280 mK", Cryogenics, **40**, pp. 685-691, 2001.
3. P.D. Mauskopf, J.J. Bock, H. del Castillo, W.L. Holzapfel, and A.E. Lange, "Composite infrared bolometers with Si_3N_4 micromesh absorbers", Appl. Optics, **36**, pp. 765-771, 1997.
4. J. Glenn, G. Chattopadhyay, S.F. Edgington, A.E. Lange, J.J. Bock, P.D. Mauskopf, A.T. and Lee. "Numerical Optimization of Integrating Cavities for Diffraction Limited Millimeter-Wave Bolometer Arrays". Applied Optics, **41**, pp. 136-142, 2002.
5. E. Serabyn, "A Wide-Field Relay Optics System for the Caltech Submillimeter Observatory", Int. Jour. Infrared & MM Waves, **18**, pp. 273-184, 1997.
6. J. C. Mather, "Bolometer noise: nonequilbrium theory", Appl. Opt., **21**, pp. 1125-1129 (1982).
7. J-M. Lamarre, "Photon noise in photometric instruments at far-infrared and submilliemeter wavelengths", Appl. Opt., **25**, pp. 870-876 (1986).